

# Modulating Electrolyte Solvation Structure for High-Voltage and Low-Temperature Magnesium-Ion Supercapacitors

Xiaohong Tan<sup>+</sup><sup>[a]</sup> Chi Fang<sup>+</sup><sup>[c]</sup> Zhongqi Liang,<sup>[a]</sup> Zhengjie Xu,<sup>[a]</sup> Jixin Zheng,<sup>[c]</sup> Xianqi Xu,\*<sup>[c]</sup> Yufeng Jin,<sup>[a]</sup> Guoshen Yang,\*<sup>[b]</sup> and Hang Zhou<sup>\*[a]</sup>

Aqueous supercapacitors have great potential in energy storage devices due to their high-power density and safety. However, due to the water hydrogen evolution reaction (HER) and oxygen evolution reaction (OER), the electrochemical stabilization window of aqueous electrolytes needs to be widened. Moreover, the application of aqueous electrolyte at low temperature is often limited by the freezing point of water. In this paper, we modulate the solvation structure of aqueous magnesium-ion supercapacitors by using sulfolane as a co-solvent. The modulated low salt concentration hybrid electrolyte extends the electrochemical stability window of the electrolyte to 2.9 V and enhances the stability of the electrolyte at extreme temperatures, as well as provides safe and non-flammable properties. Based on the hybrid electrolyte, the water-organic

hybrid magnesium-ion supercapacitors (HMSCs) are able to operate within an enlarged voltage range of 0–2.2 V at a low temperature of –30 °C. The HMSC shows a specific capacitance of up to 58 F/g at room temperature and retains a specific capacitance of 39 F/g at a current density of 15 A/g, demonstrating a good rate performance. Furthermore, after 15,000 cycles at a charge/discharge current density of 5 A/g, the HMSC sustain 88% specific capacitance. It also has an outstanding cycling performance at –30 °C, maintaining a specific capacitance of more than 92% after 20,000 cycles. These findings suggest that modulating the solvation structure by organic solvent additive is an effective solutions enabling high-voltage and low-temperature aqueous supercapacitors.

## Introduction

The rapid development of high-efficiency and high-safety energy storage systems has been driven by the rising demand for renewable energy sources, electric vehicles, and portable electronic devices.<sup>[1]</sup> Supercapacitors (SCs), or electrical double-layer capacitors hold great potential as energy storage systems due to their ability to deliver high power output and ultralong lifetime. In commercial supercapacitors, organic electrolytes are commonly employed because of their broad electrochemical stability window (ESW) which enables a high operation voltage and enhanced energy density.<sup>[2]</sup> Nevertheless, high cost as well as the flammability and environmental unfriendliness of organic electrolytes bring in cost and safety concerns. Compared to

organic electrolytes, aqueous electrolytes have low-cost and inherent safety, which is a promising approach to fundamentally tackle the above problems. However, the narrow ESW of aqueous solution (above 1.23 V for water decomposes) seriously reduces the energy density of aqueous supercapacitor, which limit their practical application.<sup>[3]</sup> Therefore, broadening the ESW of the aqueous electrolyte is highly significant for achieving high energy density aqueous supercapacitor.

Extensive research has been conducted to extend the ESW of aqueous electrolytes in order to resolve the challenges they face, such as acidic–alkaline dual electrolytes,<sup>[4]</sup> electrolytes with redox additives,<sup>[5]</sup> high-concentration electrolytes,<sup>[6]</sup> and hybrid electrolytes with organic co-solvents.<sup>[7]</sup> The acidic alkaline dual electrolyte system can regulate the pH value of the catholyte/ anolyte through an ion-selective membrane to inhibit the hydrogen evolution reaction (HER) and oxygen evolution reaction (OER) within water<sup>[8]</sup> in both electrodes, achieving a wider ESW of aqueous electrolyte. Nonetheless, the complicated cell structure and expensive bipolar membrane hamper its widespread applications. Recent studies have demonstrated the addition of redox couples near the water-splitting potential could effectively inhibit HER/OER and achieve the widen ESW of aqueous electrolytes.<sup>[9]</sup> However, the wider ESW with redox-active electrolytes in aqueous devices also faces the challenge of severe self-discharge, which can ultimately result in degradation of performance in aqueous devices. Raising the salt concentration, thereby reducing the free water molecules, is another efficacious strategy for expanding the equivalent ESW for the aqueous electrolyte.<sup>[10]</sup> For instance, Suo et al. first

[a] X. Tan,<sup>+</sup> Z. Liang, Z. Xu, Y. Jin, H. Zhou  
School of Electronic and Computer Engineering, Peking University Shenzhen Graduate School, 2199 Lishui Rd, Shenzhen 518055, China  
E-mail: zhoudh81@pkusz.edu.cn

[b] G. Yang  
School of Information Science and Engineering, Shandong University, 72 Binhai Road, Qingdao 266237, China  
E-mail: yangguoshen@sdu.edu.cn

[c] C. Fang,<sup>+</sup> J. Zheng, X. Xu  
School of Advanced Materials, Peking University Shenzhen Graduate School, 2199 Lishui Rd, Shenzhen 518055, China  
E-mail: xuxianqi@pku.edu.cn

[+] These authors contribute equally to this work.

Supporting information for this article is available on the WWW under <https://doi.org/10.1002/batt.202400620>

reported highly-concentrated 21 M LiTFSI electrolyte called “water in salt (WIS)”, which shows a broad ESW of 3 V.<sup>[6a]</sup> Although WIS electrolytes have been frequently applied in aqueous electrochemical energy storage (AEES) devices. However, the use of highly-concentrated salts inevitably leads to increased costs, elevated viscosity, and diminished ion conductivity, which in turn adversely affects the power performance of the device and impair its practicability. Recently, it was also reported that the addictive organic solvent in high-concentration electrolyte can significantly improve the ion diffusion, reduces salt amount and maintain the wide ESW of the hybrid electrolyte.<sup>[3b,7b,11]</sup>

Besides expanding the ESW of the aqueous electrolyte, the development of high energy density supercapacitor working at low temperatures is still a challenge.<sup>[12]</sup> With temperature decreasing, the performance of supercapacitors is swiftly diminished due to a significant decline in ionic conductivity caused by the freezing of aqueous electrolytes, which in turn impedes the application of conventional aqueous supercapacitors.<sup>[13]</sup> Therefore, the key to achieving aqueous supercapacitors with a wide temperature operating range is to develop electrolytes with anti-freezing property and thermal stability. At low temperatures, the solidification of an aqueous electrolyte involves a shift from a state of disorganized water molecules to a structured arrangement of ice crystals. This transition is propelled by the establishment of a coherent framework of hydrogen bonds within the ice lattice. A viable approach to prevent the solidification of water is to disrupt the hydrogen-bonding network formed by water molecular. To date, a variety of effective solutions for suppressing the freeze of aqueous electrolyte have been reported to enhance low-temperature performances of aqueous electrochemical energy storage devices, such as high-concentration electrolytes,<sup>[14]</sup> hydrogel electrolytes,<sup>[15]</sup> and electrolytes with co-solvents.<sup>[16]</sup> However, these solutions also introduce several challenges, such as the higher cost and lower ionic conductivity associated with high-concentration metal salts, environmental concerns regarding the use of organic additives in electrolytes, and the complexity and high cost of fabricating hydrogel electrolytes.<sup>[17]</sup> Therefore, reducing water activity of aqueous electrolyte are crucial. Based on the above description, the electrolyte with organic co-solvent is expected to become an effective approach to synchronously address ESW and working temperature range issues in aqueous electrolytes. Still, the impact of various organic solvent types and the molar ratios between salt, water and solvent on the physical and chemical properties of the hybrid electrolytes remains unexplored.<sup>[18]</sup> To engineer better aqueous supercapacitors that have exceptional comprehensive performance, including safety, high operation voltage, low-temperature tolerance and high energy density, a thorough understanding of the alterations in the properties of hybrid electrolytes with varying compositions and corresponding ratios is imperative.

Herein, we report a water-organic hydrous high-voltage electrolyte composed of Mg(ClO<sub>4</sub>)<sub>2</sub> salt and sulfolane(SL) solvent. As a low toxicity, low-cost and thermally stable co-solvent, SL has a strong interaction with water molecules and

can effectively reduce water activity. SL has been reported as a hydrogen bond acceptor that effectively inhibits the hydrogen evolution reaction in aqueous electrolytes,<sup>[19]</sup> helping to achieve an electrochemical stable window. Additionally, SL has the potential to form a deep eutectic system with salts,<sup>[20]</sup> lowering the freezing point. Molecular dynamics (MD) simulations verifies that SL inhibits the decomposition of water by participating in the solvation sheath layer of Mg<sup>2+</sup> and disrupting the hydrogen bonds network of water molecules. The ESW of the magnesium ion electrolyte containing 50% SL solvent (MS<sub>0.5</sub> electrolyte) is extended to 2.9 V. At the same time, the freezing behavior of the electrolyte at low temperature is inhibited due to the disturbance of the hydrogen bonds inside the water molecules, improving the low temperature resistance, and the glass transition temperature of the electrolyte is as low as -99 °C. As a result, the prepared hybrid magnesium supercapacitor has a high voltage of 2.2 V at -30 °C and exhibits a long-term cycling stability after 20,000 cycles at 5 A/g, maintaining a 91% capacitance retention.

## Results and Discussion

### Material Characterization

In experiments, 2 M Mg(ClO<sub>4</sub>)<sub>2</sub> electrolyte was prepared using a series of water and SL hybrid solvents to investigate the effect of the sulfolane (SL) on the electrolyte, and to identify the optimal electrolyte ratio. The mixed electrolyte with a solvent volume ratio of SL: H<sub>2</sub>O<sub>1-x</sub> (x=0, 0.25, 0.5, 0.75, 0.9) solvent was indicated as MS<sub>x</sub>, where x denotes the volume fraction of the SL in the total mixed solvent.

Confining by the HER/OER of water, the electrochemical stable window (ESW) reveals the electrochemical stability of the electrolyte. The ESW of electrolytes was assessed by electrochemical linear sweep voltammetry (LSV) in a three-electrode system. As depicted in Figure 1a, the ESW of 2 M Mg(ClO<sub>4</sub>)<sub>2</sub> electrolyte is 2.13 V while the electrolytes of MS<sub>0.25</sub>, MS<sub>0.5</sub>, MS<sub>0.75</sub> and MS<sub>0.9</sub> demonstrate a ESW of 2.47 V, 2.92 V, 3.47 V, and 4.62 V, respectively. It is interesting note that although SL is flammable,<sup>[20]</sup> the mixed electrolyte is non-flammable. As shown in Figure 1b, pure SL burns after 24 s with fire, while the mixed solution is non-flammable until after 90 s. After 90 s, the fiberglass paper with MS<sub>0.9</sub> solution was curled, and the fiberglass paper with MS<sub>0.5</sub> electrolyte did not change at all. Figure S1 shows that the electrolyte is non-flammable even when the SL content is as high as 90%. In Figure S2, it is found that the modulated electrolyte improves the electrochemical stability of electrolytes and ensuring safety. The strong interaction of SL and H<sub>2</sub>O can inhibit the evaporation of H<sub>2</sub>O (Figure S3). The ionic conductivity of the electrolyte was analyzed according to the Nyquist plot of electrochemical impedance spectroscopy (EIS) at different temperatures in Figures S4 and S5. In Figures 1c and S4, with the increasing concentration of SL, the ionic conductivity of the electrolytes decreases, while the viscosity increases obviously in MS<sub>0.75</sub> (13.08 mS/cm) and MS<sub>0.9</sub> (0.6 mS/cm). The above tests suggest

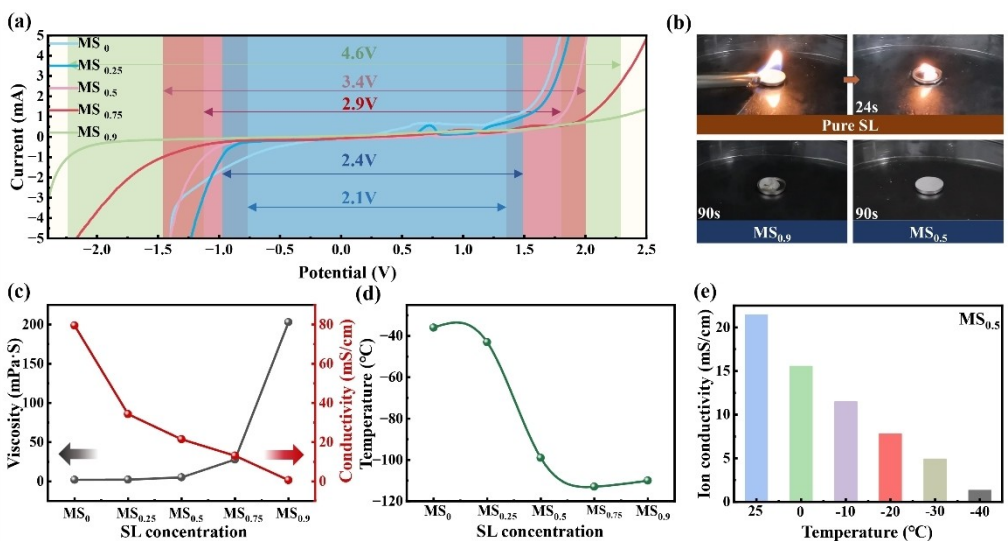


**Figure 1.** (a) Electrochemical stability windows for 2 M MS<sub>x</sub> ( $x = 0, 0.25, 0.5, 0.75, 0.9$ ) determined by LSV tests at a scan rate of 2 mV/s. (b) Ignition test s of pristine glass fiber separators saturated with MS<sub>0.5</sub> electrolyte and SL. (c) Conductivity and viscosity of MS<sub>x</sub> electrolytes with different salt-to-sulfolane volume ratios. (d) The freezing point of different electrolytes. (e) The ion conductivity of the MS<sub>0.5</sub> electrolyte at 25 °C, 0 °C, -10 °C, -20 °C, -30 °C and -40 °C.

that electrolytes with little SL would still freeze at low temperatures and have a limited voltage window, whereas the electrolyte with too high content of SL has a high viscosity and a low ionic conductivity. The flame retardancy is weakened when there is too much SL. Therefore, the MS<sub>0.5</sub> electrolyte was selected as the target electrolyte for further analysis. Considering the balance between ionic conductivity and ESW of the electrolyte, the MS<sub>0.5</sub> electrolyte with a conductivity of 21.46 mS/cm was chosen for further physical characterization and electrochemical testing. Figure S6 shows the freezing state of different electrolytes at different temperatures, indicating that an increased addition of SL leads to a decrease in the

electrolyte's freezing temperature. The MS<sub>0.5</sub> electrolyte still remains liquid at -40 °C while the result of differential scanning calorimetry (DSC) test (as shown in Figures 1d and S7) showed that its freezing point is as low as -99 °C. Figure 1e depicts the variation in ionic conductivity from 25 °C to -40 °C, indicating a gradual decline in ionic conductivity with decreasing temperatures. The ion conductivity remains 4.93 mS/cm, 1.34 mS/cm at -30 °C and -40 °C, demonstrating potential for applications in cold conditions.

To further investigate the internal interactions within the electrolyte, structural changes were analyzed using Raman spectroscopy. In Figure 2a, the peaks between 2500 cm<sup>-1</sup> and

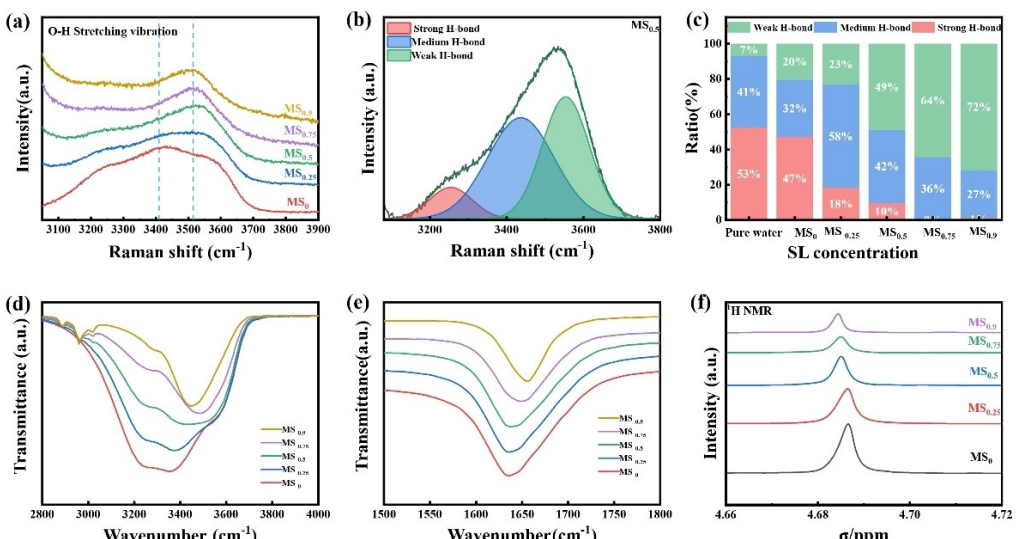


**Figure 2.** (a) The Raman spectra of the 2 M Mg(ClO<sub>4</sub>)<sub>2</sub> aqueous electrolyte MS<sub>x</sub> with different percentage of SL, as well as pure water and pure SL. (b) The fitting peaks of the three types of hydrogen bond of water in 2 M MS<sub>0.5</sub> electrolytes. (c) The hydrogen bonds in the various electrolytes and their corresponding percentages, according to the data extracted from the peak areas in the Raman spectra. (d–e) The FT-IR spectra of the MS<sub>x</sub>, as well as pure water and pure SL in 2800–400 cm<sup>-1</sup> and 1500–1800 cm<sup>-1</sup>. (f) The <sup>1</sup>H NMR spectra.

$4000\text{ cm}^{-1}$  correspond to the O–H stretching vibration modes in water.<sup>[21]</sup> Due to the presence of numerous water molecule clusters, the symmetric O–H ( $3200\text{ cm}^{-1}$ ) and the asymmetric O–H ( $3400\text{ cm}^{-1}$ ) stretching vibration modes exhibit broad Raman bands in pure water.<sup>[22]</sup> In 2 M  $\text{Mg}(\text{ClO}_4)_2$  solution a higher Raman shift is observed with a peak around  $3432\text{ cm}^{-1}$ , and this phenomenon can be ascribed to the interaction between water molecules and magnesium ions ( $\text{Mg}^{2+}$ ). Subsequently, with the incorporation of SL, a notable narrowing and sharpening of the peak corresponding to the O–H stretching vibration of water molecules is observed, accompanied by a shift to a higher Raman shift. As the SL concentration increases to  $\text{MS}_{0.5}$ , the formation of new hydrogen bonds between  $\text{H}_2\text{O}$  and SL within the electrolyte results in the O–H stretching vibration peak of water shifting to a higher Raman shift to  $3533\text{ cm}^{-1}$ . The sharper peak indicates a reduction in free water molecule clusters in the electrolyte with the addition of SL. As shown in Figures 2b and S8, the Raman spectra can be further categorized into three types of hydrogen bonds: strong H-bond at around  $3200\text{ cm}^{-1}$  and  $3400\text{ cm}^{-1}$ , which represent intra-molecular hydrogen bonds in water, and weak H-bond at around  $3600\text{ cm}^{-1}$  representing interactions between SL and  $\text{H}_2\text{O}$ .

In Figure 2c, an increase in SL content correlates with a decrease in the ratio of strong hydrogen bonds, while that of weak hydrogen bonds increases, suggesting that the introduction of SL significantly diminishes the hydrogen bonding strength between water molecules. The formation of large-scale hydrogen bond networks has been broken, thereby alleviates water freezing. Additionally, the original 2 M  $\text{Mg}(\text{ClO}_4)_2$  electrolyte exhibits characteristic peaks associated with the  $\text{ClO}_4^-$  groups' change can also be found at  $461\text{ cm}^{-1}$ ,  $628\text{ cm}^{-1}$ , and  $934\text{ cm}^{-1}$ . With the increase of SL in the solution, the bond at approximately  $461\text{ cm}^{-1}$  interacts with the SL's bonds, causing a shift in the peak.

The Fourier-transform infrared (FTIR) spectroscopy characterizations was conducted in Figure 2d for furthermore investigation. It shows that the  $\text{MS}_0$  electrolyte has a wider peak of O–H stretching ( $3200\text{ cm}^{-1}$ – $3600\text{ cm}^{-1}$ ) than  $\text{MS}_{0.5}$  electrolyte, suggesting that there are more water clusters in  $\text{MS}_0$  electrolyte. And the pure water displays a peak at approximately  $1650\text{ cm}^{-1}$ , which remains at a consistent position but narrows progressively with the increasing SL content, corresponding to a reduction in types of hydrogen bonds in water molecules. Conversely in Figure 2e, with the increase of SL content, the peak around  $1650\text{ cm}^{-1}$  narrows symmetrically, indicating a more homogeneous molecular environment as shown in the normalized band. This suggests a reduction in the variety of water molecule types of water molecules with high SL concentrations, indicating more uniform interactions with SL compared to lower SL concentrations. The  $^1\text{H}$  nuclear magnetic resonance (NMR) spectroscopy results for the electrolytes are depicted in Figure 2f. The spectra indicate that the  $^1\text{H}$  NMR signals of  $\text{H}_2\text{O}$  exhibit no significant change to the content of SL and show a negligible shift. In conclusion, the results of Raman and FTIR analyses show that SL can progressively diminish the existit of free water in the electrolyte as a hydrogen bond

acceptor. There are almost no free water molecule in  $\text{MS}_{0.5}$  electrolyte, explaining the phenomena of the wide voltage window and lowered freezing point caused by SL additive.

To further investigate the impact of SL on the electrolyte's internal structure, molecular dynamics (MD) simulations were conducted. As shown in Figure 3a, the electrolyte displays a congested state both prior to and following the addition of SL, upon reaching quasi-equilibrium, suggesting that the additional SL disrupts the hydrogen bonding formed between free water molecules within the electrolyte. To elucidate the local H-bond coordination of water molecules, simulations assessing the number of hydrogen bonds across various electrolytes were conducted, as depicted in Figure 3b. In the  $\text{MS}_0$  electrolyte, the highest proportion of water molecules, 33%, forms four hydrogen bonds capable of a quasi-tetrahedral arrangement, closely related to ice nucleation.<sup>[23]</sup> This is followed by water molecules forming three hydrogen bonds. With increasing SL content, there is a rise in the number of water molecules exhibiting 0, 1, and 2 H-bond coordinations, indicating that SL disrupts the tetrahedral hydrogen bonding network. This disruption hinders ice nucleation kinetics, leading to a reduced freezing point for the solution. The radial distribution function (RDF) results in Figure 3c reveal that the distances between  $\text{Mg}^{2+}$  and O ( $\text{H}_2\text{O}$ ), Mg and O ( $\text{ClO}_4^-$ ), and Mg and O (SL) are comparable, suggesting that these species are all involved in the primary solvation shell and contribute to  $\text{Mg}^{2+}$  coordination. Utilizing the average molecular density  $g(r)$ , the average molecular formula of the solution is inferred to be  $\text{Mg}(\text{H}_2\text{O})_{4.5}(\text{ClO}_4^-)_{0.72}(\text{SL})_{0.78}$ . To further examine the binding interactions among groups within the solution, binding energy calculations were conducted. As illustrated in Figure 3d, the binding energy comparisons reveal the extent to which various ions disrupt hydrogen bond formation between water molecules. Specifically, the SL- $\text{H}_2\text{O}$  binding energy is lower, facilitating SL's interaction with water molecules and the subsequent disruption of the hydrogen bond network. This interaction confers advantages such as a lower operating temperature and an expanded voltage range. The solvation shell structure of  $\text{Mg}^{2+}$  in the  $\text{MS}_{0.5}$  electrolyte was further characterized, identifying seven predominant structures:  $\text{Mg}(\text{H}_2\text{O})_3(\text{ClO}_4^-)(\text{SL})_2$ ,  $\text{Mg}(\text{H}_2\text{O})_4(\text{SL})_2$ ,  $\text{Mg}(\text{H}_2\text{O})_4(\text{ClO}_4^-)(\text{SL})$ ,  $\text{Mg}(\text{H}_2\text{O})_4(\text{ClO}_4^-)_2$ ,  $\text{Mg}(\text{H}_2\text{O})_5(\text{SL})$ ,  $\text{Mg}(\text{H}_2\text{O})_5(\text{ClO}_4^-)$ , and  $\text{Mg}(\text{H}_2\text{O})_6$ . An elevated energy band results in a more stable solvation configuration of  $\text{Mg}^{2+}$  within the aqueous solution, which facilitates the reconstitution of the electrolyte structure. Molecular dynamics (MD) simulations reveal that the solvation level of  $\text{Mg}^{2+}$  in a 2 M  $\text{MS}_{0.5}$  aqueous solution can be ascertained. Figure S9 demonstrates  $\text{Mg}^{2+}$  predominantly exists in the form of a  $\text{Mg}(\text{H}_2\text{O})_5\text{SL}^{2+}$  solvation shell structure within the solution. This confirms significant structure alterations in the solution compared to the  $\text{MS}_0$  electrolyte.

## Performance of HMSCs

To evaluate the efficacy of the  $\text{MS}_{0.5}$  electrolyte, a symmetric hybrid-electrolyte magnesium-ion supercapacitor (HMSC) was

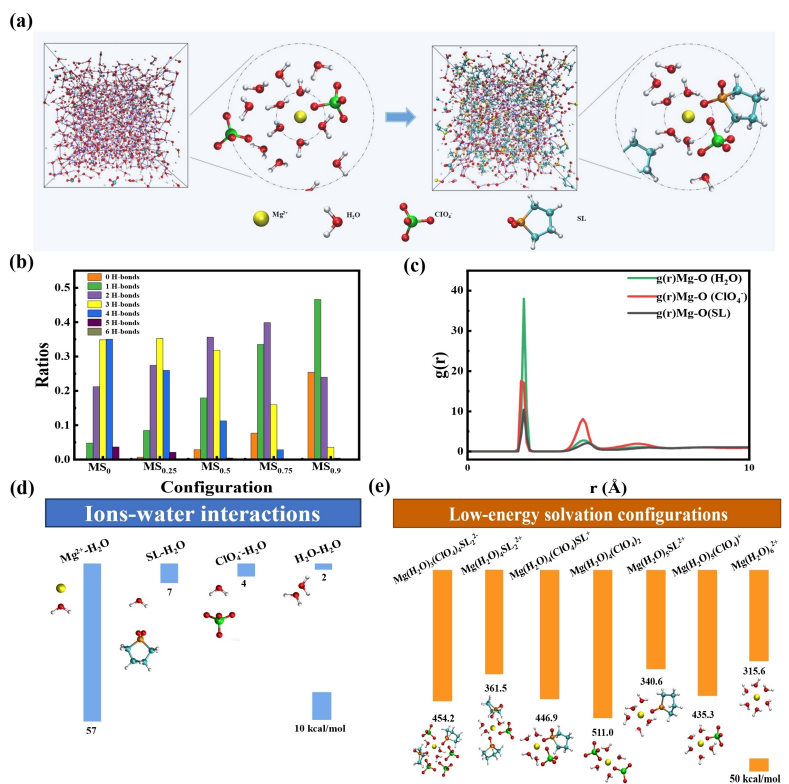


**Figure 3.** (a) Snapshots corresponding to the solvation structures of 2 M  $MS_0$  electrolytes and 2 M  $MS_{0.5}$  electrolytes. (b) The proportions of hydrogen bonds among various quantities in water molecules. (c) The RDF and coordination numbers ( $Mg^{2+}$  as the center) of  $Mg-O(H_2O)$ ,  $Mg-O(ClO_4^-)$  and  $Mg-O(SL)$ , corresponding to the 2 M  $MS_{0.5}$  electrolytes. (d) The energies associated with the binding of ions to water molecules, as well as the energies required for the formation of solvation structures around  $Mg^{2+}$  ions.

constructed, employing two YP-50 F electrodes. As depicted in Figure 4a, The HMSC with the 2 M  $MS_{0.5}$  electrolyte displayed a high stable voltage of 2.2 V, which is 0.5 V higher than that of the 2 M  $MS_0$  HMSC, while the coulombic efficiency of the capacitor remained above 95 %, indicative of good reversibility. Figure 4b presents the curves obtained from galvanostatic charge-discharge (GCD) tests at varying current densities, exhibiting symmetric triangular capacitive behavior.<sup>[26]</sup> Figure 4c illustrates the specific capacity of the 2 M  $MS_{0.5}$  HMSC at various current densities at 25 °C. With an increase in current density from 0.5 A/g to 15 A/g, the specific capacity of the capacitor decreased from 58 F/g to 39 F/g, reflecting excellent rate capability. The SCs using  $MS_{0.5}$  electrolyte have an improved specific capacitance compared to those using  $MS_0$  at various current densities as shown in Figure S10. The Ragone plots in Figure 4d is utilized to assess the power and energy density of the  $MS_{0.5}$  HMSC device.<sup>[27]</sup> The aqueous HMSC demonstrates an attractive energy density of 26.27 Wh/kg and a power density of 223 kW/kg at room temperature, which is higher than that of most reported aqueous magnesium-ion supercapacitors (Table S1).<sup>[25b,28]</sup> Furthermore, Figure 4e indicates that the 2 M  $MS_{0.5}$  HMSC sustained a capacity retention rate exceeding 88 % and a coulombic efficiency above 95 % after 15000 cycles at a current density of 5 A/g, demonstrating outstanding cycling performance.<sup>[29]</sup> These findings suggest that the supercapacitor

with the  $MS_{0.5}$  electrolyte exhibits superior rate performance and cycling stability over a voltage range of 0 V to 2.2 V.

Furthermore, to explore the electrolyte's performance at low temperatures, electrochemical tests were conducted on the devices over a range of temperatures. Moreover, the low-temperature electrical performance of the supercapacitor was assessed, as shown in Figure S11. It can be observed in Figure 4f that the specific capacitance of the 2 M  $MS_{0.5}$  HMSC reduced from 58 F/g at 25 °C to 16.3 F/g at -30 °C. Figure 4g presents the specific capacity of the 2 M  $MS_{0.5}$  HMSC at various current densities at -30 °C. With an increasing current density from 0.5 A/g to 15 A/g, the specific capacity of the capacitor decreased from 16.3 F/g to 6.3 F/g. Furthermore, it maintained a capacity retention rate exceeding 92 % with a coulombic efficiency approaching 100 % after 20,000 cycles at a current density of 5 A/g, as illustrated in Figure 4i, demonstrating outstanding cycling performance under low temperature. Compared to other ion supercapacitors (Table S2),<sup>[30]</sup> it exhibits a notable energy density of 11 Wh/kg and a power density of 2 kW/kg at -30 °C, as depicted in Figure 4h,<sup>[8,24,27b,30,31]</sup> Nonetheless, it retained good capacitive performance, underscoring the device's suitability for low-temperature applications.

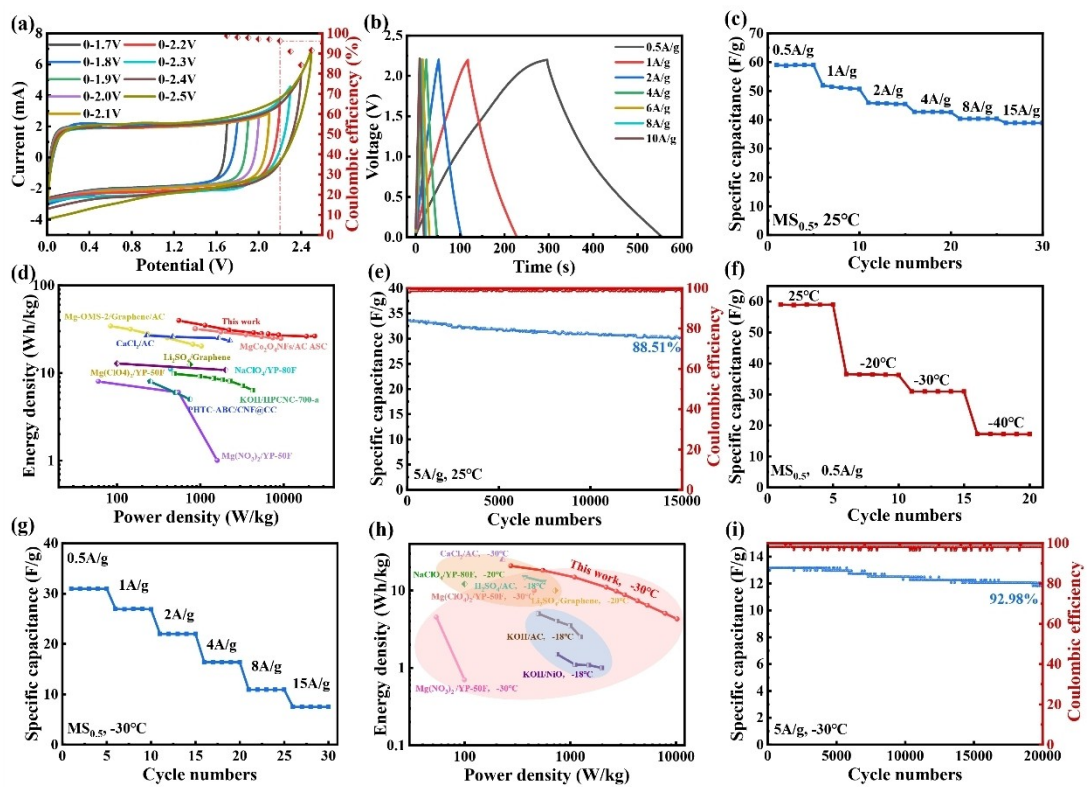


**Figure 4.** (a) The cyclic voltammetry (CV) curves of the HMSC with 2 M MS<sub>0.5</sub> electrolyte under different voltage window at 5 mV/s. (b) The GCD curves of HMSC with 2 M MS<sub>0.5</sub> electrolyte under different current densities at 25 °C. (c) The specific capacity of HMSC with 2 M MS<sub>0.5</sub> electrolyte under different current densities at 25 °C. (d) Ragone plot of the HMSC with 2 M MS<sub>0.5</sub> electrolyte and other aqueous supercapacitors at 25 °C.<sup>[24]</sup> (e) The cycle performance of and coulombic efficiency of HMSC with 2 M MS<sub>0.5</sub> electrolyte at 5 A/g, 25 °C. (f) The specific capacity of HMSC with 2 M MS<sub>0.5</sub> electrolyte under different temperatures at 0.5 A/g. (g) The rate performance of the HMSCs at various current densities at -30 °C. (h) The Ragone plot of the HMSC with 2 M MS<sub>0.5</sub> electrolyte and other aqueous Mg-ion supercapacitors at -30 °C.<sup>[24,25]</sup> (i) The cycle performance of and coulombic efficiency of HMSC with 2 M MS<sub>0.5</sub> electrolyte at 5 A/g, -30 °C.

## Conclusions

In summary, SL was used as a co-solvent to enhance the stability of the electrolyte, resulting in an electrolyte for high-voltage and low-temperature applications. The electrolyte is non-flammable and exhibits an electrochemically stable window of 2.92 V, remains in liquid form at -40 °C, and has a theoretical glass transition temperature as low as -99 °C. The MS<sub>0.5</sub> electrolyte was utilized in the production of supercapacitors, achieving an operating voltage of up to 2.2 V. The specific capacitance at room temperature reached 58 F/g at a current density of 0.5 A/g. Additionally, when the current density is 5 A/g, the capacity retention rate exceeded 88% after 15,000 cycles at room temperature. At -30 °C, the specific capacitance at a current density of 0.5 A/g is 16.3 F/g, which is at a high level among magnesium supercapacitors. Furthermore, at a current density of 5 A/g at -30 °C, the capacity retention rate is as high as 92% after 20000 cycles. Meanwhile, SCs utilizing other electrolyte with SL also showed higher voltage and improved performance at low temperatures in Figure S12. This study offers valuable insights for the research and development of aqueous energy storage devices operating in ultra cold conditions.

## Experimental Section

### Material Preparation

Chemical reagents: SL has been proven to act as a hydrogen bond acceptor, effectively inhibiting the hydrogen evolution reaction in aqueous electrolyte Mg(ClO<sub>4</sub>)<sub>2</sub> (AR, > 99%) was purchased from Macklin. Sulfolane (> 99.0%) and N-methyl pyrrolidone (NMP) were purchased from Aladdin Chemical Reagent Co., Ltd. YP-50F was bought from Foshan Porous Carbon Tech Co., Ltd. Polyvinylidene fluoride (PVDF) and Super P were purchased from Canrd Tech Co., Ltd. And the carbon cloth (wos1011) was bought from Ce-Tech. Co., Ltd.

Electrolytes preparation: A series of electrolytes were prepared by dissolving 2 M Mg(ClO<sub>4</sub>)<sub>2</sub> into the mixture with different H<sub>2</sub>O and sulfolane (SL) in volume ratios at room temperature.

Preparation of electrodes and assembly of supercapacitors: A mixture was created for the fabrication of activated carbon electrodes, comprising YP-50F as the primary material, Super P as a conductive enhancer, and polyvinylidene fluoride (PVDF) acting as a binding agent. This mixture was dissolved in N-methyl-2-pyrrolidone (NMP), maintaining a mass ratio of 7:2:1. The resulting slurry was applied to a carbon cloth substrate and subjected to drying at a temperature of 70 °C for a duration of 6 hours under vacuum conditions. The mass of the active material was approximately between 2.0 mg per square centimeter. Supercapacitors with a carbon foundation were constructed for assessing cell

performance by layering the YP-50F cathode/anode along with a 50-micrometer-thick glass fiber separator.

## Structural Characterization

Proton nuclear magnetic resonance spectroscopy was examined using a 400 MHz AVANCE NEO instrument (Bruker) with deuterated water serving as the solvent. Raman spectrometer and Fourier-transform infrared analyses were performed using a LabRAM HR800 system (Horiba Jobin Yvon, with a 532 nm laser at 10 mW power) and a Vertex70 spectrometer (Bruker), respectively. Thermogravimetric and differential scanning calorimetry measurement were examined by STA449F3 (TG-DSC, NETZSCH, 5 °C/min in a N<sub>2</sub> atmosphere).

## Electrochemical Characterization

A CHI660 electrochemical workstation from CH Instruments, Inc., was utilized to perform LSV, CV, and EIS analyses. The LSV procedure was employed to assess the ESW of the electrolytes, employing platinum as the counter electrode, while the reference electrodes were both carbon cloth. To ascertain ionic conductivity, EIS measurements were taken across a frequency spectrum extending from 100,000 Hz down to 0.01 Hz, while the AC potential was set to 5 mV. The Neware WIHW-200 L-160CH apparatus by NEWARE Co., Ltd., was employed to evaluate the capabilities and cycling endurance. The ionic conductivities were calculated by employing the subsequent formula:

$$\sigma = L / (R_s A)$$

Where the ionic conductivity, denoted by  $\sigma$  (in S/cm), is determined by the resistance of the electrolyte ( $R$ , measured in  $\Omega$ ), the contact area of the electrodes ( $S$ , in  $\text{cm}^2$ ), and the electrolyte's thickness ( $L$ , in cm), respectively.

## Acknowledgements

This work is supported by Shenzhen Science and Technology Innovation Committee (KJZD20230923113759002, KJZD20230923115005009, GJHZ20240218113959009), and the Guangdong Introducing Innovative and Entrepreneurial Teams Program (2019ZT08Z656).

## Conflict of Interests

The authors declare that they have no known competing financial interests or personal relationships that could have appeared to influence.

## Data Availability Statement

The data that support the findings of this study are available in the supplementary material of this article.

**Keywords:** Hybrid electrolyte • High operation voltage • Low temperature • Supercapacitor

- [1] a) W. Yang, W. Yang, J. Zeng, Y. Chen, Y. Huang, J. Liu, J. Gan, T. Li, H. Zhang, L. Zhong, X. Peng, *Prog. Mater. Sci.* **2024**, *144*, 101264; b) T. Sun, Q. Nian, X. Ren, Z. Tao, *Joule* **2023**, *7*, 2700–2731.
- [2] S. Wu, B. Su, M. Sun, S. Gu, Z. Lu, K. Zhang, D. Y. W. Yu, B. Huang, P. Wang, C.-S. Lee, W. Zhang, *Advanced Materials* **2021**, *33*, 2102390.
- [3] a) L. Smith, B. Dunn, *Science* **2015**, *350*, 918–918; b) D. Xiao, Q. Dou, L. Zhang, Y. Ma, S. Shi, S. Lei, H. Yu, X. Yan, *Advanced Functional Materials* **2019**, *29*, 1904136.
- [4] a) C. Liu, X. Chi, Q. Han, Y. Liu, *Advanced Energy Materials* **2020**, *10*, 1903589; b) C. Li, W. Wu, P. Wang, W. Zhou, J. Wang, Y. Chen, L. Fu, Y. Zhu, Y. Wu, W. Huang, *Advanced Science* **2019**, *6*, 1801665.
- [5] a) X. Wu, H. Yang, M. Yu, J. Liu, S. Li, *Mater. Today Energy* **2021**, *21*, 100739; b) A. Shanmugavani, S. Kaviselvi, K. V. Sankar, R. K. Selvan, *Mater. Res. Bull.* **2015**, *62*, 161–167.
- [6] a) L. Suo, O. Borodin, T. Gao, M. Olguin, J. Ho, X. Fan, C. Luo, C. Wang, K. Xu, *Science* **2015**, *350*, 938–943; b) L. Jiang, Y. Lu, C. Zhao, L. Liu, J. Zhang, Q. Zhang, X. Shen, J. Zhao, X. Yu, H. Li, X. Huang, L. Chen, Y.-S. Hu, *Nat. Energy* **2019**, *4*, 495–503.
- [7] a) Q. Dou, Y. Lu, L. Su, X. Zhang, S. Lei, X. Bu, L. Liu, D. Xiao, J. Chen, S. Shi, X. Yan, *Energy Storage Mater.* **2019**, *23*, 603–609; b) Q. Dou, S. Lei, D.-W. Wang, Q. Zhang, D. Xiao, H. Guo, A. Wang, H. Yang, Y. Li, S. Shi, X. Yan, *Energy Environ. Sci.* **2018**, *11*, 3212–3219.
- [8] L. Su, Q. Zhang, Y. Wang, J. Meng, Y. Xu, L. Liu, X. Yan, *J. Mater. Chem. A* **2020**, *8*, 8648–8660.
- [9] a) Y. Song, P. Deng, Z. Qin, D. Feng, D. Guo, X. Sun, X.-X. Liu, *Nano Energy* **2019**, *65*, 104010; b) R. Sahoo, D. T. Pham, T. H. Lee, T. H. T. Luu, J. Seok, Y. H. Lee, *ACS Nano* **2018**, *12*, 8494–8505.
- [10] J. Chen, S. Lei, S. Zhang, C. Zhu, Q. Liu, C. Wang, Z. Zhang, S. Wang, Y. Shi, L. Yin, R. Wang, *Advanced Functional Materials* **2023**, *33*, 2215027.
- [11] a) H. Zhang, B. Qin, J. Han, S. Passerini, *ACS Energy Lett.* **2018**, *3*, 1769–1770; b) F. Wang, O. Borodin, M. S. Ding, M. Gobet, J. Vatamanu, X. Fan, T. Gao, N. Eidson, Y. Liang, W. Sun, S. Greenbaum, K. Xu, C. Wang, *Joule* **2018**, *2*, 927–937.
- [12] P. Zhang, W. Zhang, Z. Wang, X. Wang, Q. Ren, S. Zhang, Y. Wang, L. He, P. Liu, Q. Zhang, Z. Shi, *eScience* **2023**, *3*, 100184.
- [13] a) G. Yang, J. Huang, X. Wan, B. Liu, Y. Zhu, J. Wang, O. Fontaine, S. Luo, P. Hiralal, Y. Guo, H. Zhou, *EcoMat* **2022**, *4*, e12165; b) G. Yang, J. Huang, X. Wan, Y. Zhu, B. Liu, J. Wang, P. Hiralal, O. Fontaine, Y. Guo, H. Zhou, *Nano Energy* **2021**, *90*, 106500.
- [14] a) D. Reber, R.-S. Kühnel, C. Battaglia, *ACS Materials Lett.* **2019**, *1*, 44–51; b) Y. Zhao, Z. Chen, F. Mo, D. Wang, Y. Guo, Z. Liu, X. Li, Q. Li, G. Liang, C. Zhi, *Adv. Sci.* **2021**, *8*, 2002590.
- [15] a) J. Bae, Y. Li, J. Zhang, X. Zhou, F. Zhao, Y. Shi, J. B. Goodenough, G. Yu, *Angew. Chem. Int. Ed.* **2018**, *57*, 2096–2100; b) G. Yang, X. Xu, G. Qu, J. Deng, Y. Zhu, C. Fang, O. Fontaine, P. Hiralal, J. Zheng, H. Zhou, *Chem. Eng. J.* **2023**, *455*, 140806.
- [16] a) A. Tron, S. Jeong, Y. D. Park, J. Mun, *ACS Sustainable Chem. Eng.* **2019**, *7*, 14531–14538; b) A. M. Haregewoin, A. S. Wotango, B.-J. Hwang, *Energy Environ. Sci.* **2016**, *9*, 1955–1988.
- [17] G. Yang, X. Xu, G. Qu, J. Deng, Y. Zhu, C. Fang, O. Fontaine, P. Hiralal, J. Zheng, H. Zhou, *Chem. Eng. J.* **2023**, *455*, 140806.
- [18] D. Xiao, Q. Dou, L. Zhang, Y. Ma, S. Shi, S. Lei, H. Yu, X. Yan, *Advanced Functional Materials* **2019**, *29*, 1904136.
- [19] a) Y. Wang, T. Wang, D. Dong, J. Xie, Y. Guan, Y. Huang, J. Fan, Y.-C. Lu, *Matter* **2022**, *5*, 162–179; b) J. Liu, C. Yang, X. Chi, B. Wen, W. Wang, Y. Liu, *Advanced Functional Materials* **2022**, *32*, 2106811; c) B. Bartokova, A. G. Marangoni, T. Laredo, E. Pensini, *Colloids and Surfaces A: Physicochemical and Engineering Aspects* **2023**, *677*, 132451.
- [20] X. Lin, G. Zhou, M. J. Robson, J. Yu, S. C. T. Kwok, F. Ciucci, *Advanced Functional Materials* **2022**, *32*, 2109322.
- [21] M. Li, X. Wang, J. Hu, J. Zhu, C. Niu, H. Zhang, C. Li, B. Wu, C. Han, L. Mai, *Angewandte Chemie International Edition* **2023**, *62*, e202215552.
- [22] Q. Zheng, S. Miura, K. Miyazaki, S. Ko, E. Watanabe, M. Okoshi, C. P. Chou, Y. Nishimura, H. Nakai, T. Kamiya, T. Honda, J. Akikusa, Y. Yamada, A. Yamada, *Angew. Chem. Int. Ed. Engl.* **2019**, *58*, 14202–14207.
- [23] Q. Sun, *Chem. Phys. Lett.* **2013**, *568–569*, 90–94.
- [24] L. Su, L. Gong, C. Ma, X. Wang, Z. Sun, *ChemElectroChem* **2017**, *4*, 46–48.
- [25] a) A. A. Mrozievicz, K. Solska, G. Z. Żukowska, M. Skunik-Nuckowska, *Batteries* **2024**, *10*, 213; b) C. You, W. Wu, W. Yuan, P. Han, Q. Zhang, X. Chen, X. Yuan, L. Liu, J. Ye, L. Fu, Y. Wu, *Advanced Functional Materials* **2023**, *33*, 2208206.

- [26] Y.-T. Hwang, H.-S. Kim, *Int. J. Precis. Eng. Manuf.-Green Technol.* **2022**, *9*, 201–211.
- [27] a) R. Vellacheri, A. Al-Haddad, H. Zhao, W. Wang, C. Wang, Y. Lei, *Nano Energy* **2014**, *8*, 231–237; b) S. Lan, C. Yu, J. Yu, X. Zhang, Y. Liu, Y. Xie, J. Wang, J. Qiu, *Small* **2024**, *n/a*, 2309286. c) H. Zhang, K. Ye, K. Zhu, R. Cang, X. Wang, G. Wang, D. Cao, *ACS Sustainable Chem. Eng.* **2017**, *5*, 6727–6735; d) H. Chen, X. Du, R. Wu, Y. Wang, J. Sun, Y. Zhang, C. Xu, *Nanoscale Adv.* **2020**, *2*, 3263–3275; e) G. Tian, P. Chai, H. Yu, W. Zheng, *J. Solid State Electrochem.* **2023**, *27*, 2771–2777.
- [28] F. Wu, M. Liu, Y. Li, X. Feng, K. Zhang, Y. Bai, X. Wang, C. Wu, *Electrochemical Energy Reviews* **2021**, *4*, 382–446.
- [29] J. Wang, J. Tang, B. Ding, V. Malgras, Z. Chang, X. Hao, Y. Wang, H. Dou, X. Zhang, Y. Yamauchi, *Nat. Commun.* **2017**, *8*, 15717.
- [30] L. Su, L. Gong, X. Wang, H. Pan, *International Journal of Energy Research* **2016**, *40*, 763–769.
- [31] J. Menzel, E. Frackowiak, K. Fic, *J. Power Sources* **2019**, *414*, 183–191.

Manuscript received: September 20, 2024

Revised manuscript received: October 25, 2024

Accepted manuscript online: October 30, 2024

Version of record online: November 20, 2024